HART-II Acoustic Predictions using a Coupled CFD/CSD Method

D. Douglas Boyd, Jr.
Research Aerospace Engineer
NASA Langley Research Center
Hampton, Virginia 23681-2199
David.D.Boyd@nasa.gov

American Helicopter Society 65th Annual Forum
May 27-29, 2009
Grapevine, Texas

Abstract

This paper documents results to date from the Rotorcraft Acoustic Characterization and Mitigation activity under the NASA Subsonic Rotary Wing Project. The primary goal of this activity is to develop a NASA rotorcraft impulsive noise prediction capability which uses first principles fluid dynamics and structural dynamics. During this effort, elastic blade motion and co-processing capabilities have been included in a recent version of the computational fluid dynamics code (CFD). The CFD code is loosely coupled to computational structural dynamics (CSD) code using new interface codes. The CFD/CSD coupled solution is then used to compute impulsive noise on a plane under the rotor using the Ffowcs Williams-Hawkings solver. This code system is then applied to a range of cases from the Higher Harmonic Aeroacoustic Rotor Test II (HART-II) experiment. For all cases presented, the full experimental configuration (*i.e.*, rotor and wind tunnel sting mount) are used in the coupled CFD/CSD solutions. Results show good correlation between measured and predicted loading and loading time derivative at the only measured radial station. A contributing factor for a typically seen loading mean-value offset between measured data and predictions data is examined. Impulsive noise predictions on the measured microphone plane under the rotor compare favorably with measured mid-frequency noise for all cases. Flow visualization of the BL and MN cases shows that vortex structures generated in the prediction method are consist with measurements. Future application of the prediction method is discussed.

Introduction

Under the NASA Fundamental Aeronautics Program Subsonic Rotary Wing (SRW) Project, rotorcraft acoustics is one of the key research areas. Though this research area covers many related activities, in this document, only a portion of the Rotorcraft Acoustic Characterization and Mitigation activity is addressed. A major goal of this activity is to implement a NASA rotorcraft impulsive noise (acoustic) prediction capability which uses first principles fluid dynamics and structural dynamics. This method is intended to improve NASA's impulsive noise prediction capabilities for several phases of rotorcraft flight. Specifically, this method will improve prediction capabilities for High Speed Impulsive (HSI) noise in high speed forward flight and for Blade Vortex Interaction (BVI) noise in low speed descending flight. The current activity focuses on the implementation of this method with regard to BVI noise prediction capability.

Presented at the American Helicopter Society 65th Annual Forum, Grapevine, Texas, May 27-29, 2009.

Background

Rotorcraft BVI noise has been a subject of intense research for several decades as it can be a dominant noise source during descent and landing operations. BVI noise results from close and strong interactions between the rotor blades and the rotor blade wakes. Development of methods to control this noise component will require knowledge of the underlying physics of the interaction, including the loads experienced by the blades, the wake structures generated, etc. Many efforts, past and present, have focused on modeling BVI events using "comprehensive" rotorcraft analyses. These methods typically couple structural, aerodynamics, and flight dynamics models. The structural models (i.e., "computational structural dynamics models" or "CSD") usually consist of advanced beam models which are well suited for modeling rotor blades. Modeling of aerodynamics in comprehensive analyses traditionally consists of a combination of lifting line theory, vortex wake theory, thin airfoil theory, etc. These aerodynamics models require a level of empiricism to "tune" the results to match

measured data. For example, the vortex core size in a vortex wake model determines (among other things) the maximum vortex induced loading on a rotor blade. This is parameter determined from experiment or from "trial-and-error" and can be adjusted to effectively limit, or set, the vortex induced loading on the rotor blades to match measured data.

Some examples of this "comprehensive analysis" approach previously used by NASA include methods such as CAMRAD.Mod1/HIRES [Ref. 1], TRAC [Ref. 2], and CARMA [Ref. 3]. The CAMRAD.Mod1/HIRES method was developed during the late-1980s to mid-1990s. This code was a highly modified version of the original CAMRAD code [Ref. 4, 5] designed to extract aerodynamic loading information at a high resolution necessary for impulsive noise calculations in the discrete frequency noise code, WOPWOP [Ref. 6]. The early success of this type of method was carried over into the Tilt-Rotor Aeroacoustics Code (TRAC). The TRAC – a set of codes and interfaces – was developed in the late-1990s to early-2000s. It began as upgrades to the CAMRAD.Mod1/HIRES model, and then added the ability to interface with other codes such as the full potential code, FPXBVI [Ref. 7], a modified version of WOPWOP known as WOPMOD, and the Rotorcraft Noise Model (RNM) [Ref. 8]. In the early-2000s, the Comprehensive Analytical Rotorcraft Model for Acoustics (CARMA) code system was in development. This method replaced the CAMRAD.Mod1/HIRES code with CAMRAD-II [Ref. 9], employed new interfaces between CAMRAD-II and WOPMOD, included new interfaces to the emerging PSU-WOPWOP [Ref. 10, 11] code, and included new interfaces from both WOPMOD and PSU-WOPWOP to the RNM code.

While the efforts to improve the pure comprehensive analysis approach have been successful, there have historically been limitations to these methods. For example, there is almost universal use of simplified aerodynamics models. Though these simplified aerodynamics models work well for some applications, they tend to have trouble producing the desired loading resolutions and generality necessary to account for shocks and BVI events in noise calculations.

Efforts to drastically improve and generalize the aerodynamic modeling by eliminating as much empiricism as possible involve replacing the lower order, simplified aerodynamic models with "first principles" computational fluid dynamics (CFD). There has been an impressive series of efforts to develop coupled methods for the CSD and CSD over the last two decades. Datta, et al [Ref. 12] provides an excellent historical review of these efforts. In more recent efforts, significant advances in CFD / CSD coupling were made by Lim, et al [Ref. 13] at the U.S. Army Aeroflightdynamics Directorate. Reference 13 lays much of the ground work for coupling of OVERFLOW2 and CAMRAD-II. The current work is intended to build on these past successes.

In the current effort, loose coupling of appropriate CFD, CSD, and acoustic models, using the most current available computer codes, provides a noticeable improvement in noise prediction capability. These codes, methods, and results are discussed below.

Prediction Method

Introduction

The prediction method uses a loosely coupled set of CFD, CSD, and acoustic prediction tools as shown in the schematic in Figure 1. It is similar to methods used in the past by other researchers as discussed in subsequent sections.

It should be noted first that the CFD method (OVERFLOW2 [Ref. 15]) defines blade motion as elastic motion increments added to a "reference" blade geometry. First, a rigid blade calculation (designated as "CAMRAD-II (Reference)" in Figure 1) is performed to provide a solution for the reference blade geometry motion. Second, an elastic blade calculation is performed (designated as "CAMRAD-II (Elastic) in Figure 1) for the deforming blade geometry. For these initial CAMRAD-II executions, a simple momentum inflow ("uniform inflow") is used simply to provide an initial trim and elastic blade motions. It is not necessary to execute a full CAMRAD-II free-wake trim solution because the aerodynamics will eventually be completely replaced with CFD aerodynamics.

An interface code, called "gen_motion_for_cfd", examines both the reference blade motion solution and the elastic blade motion solution, and then generates a file containing elastic blade motions relative to the reference blade solution suitable for input to OVERFLOW2. This blade motion data contains the definition of the reference blade quarter chord geometry as well as a table of three displacements and three rotation angles at discrete spanwise locations along the entire blade span for a full rotor revolution. Internal to OVERFLOW2, these deflections and rotation angles are transferred to the blade surface grids and volume grids to effect elastic motion of these entities. With this information, OVERFLOW2 is executed for a particular period of time so that aerodynamic forces can be determined for the elastically moving blades. At the end of this time period, another interface code, "gen_delta_for_cii", examines the airloads from OVERFLOW2 and CAMRAD-II, and then generates a CAMRAD-II "delta airloads" table [Ref. 9]. This table is returned to CAMRAD-II for another elastic blade / trim calculation, as discussed in detail by Potsdam, et al [Ref. 14]. As the iterations progress, the internal CAMRAD-II airloads are gradually replaced with OVERFLOW2 integrated airloads. Once the iteration cycle has converged, there is consistency between the blade motions from CAMRAD-II and airloads from OVERFLOW2.

During this study, it was determined sufficient and efficient to execute OVERFLOW2 for an interval equal to one-quarter of a rotor revolution between each CAMRAD-II trim execution. A converged trim solution was obtained after

three full rotor revolutions of OVERFLOW2. As a final step, one full additional rotor revolution of OVERFLOW2 was executed using the elastic blade motion from the final CAMRAD-II iteration. These four complete rotor revolutions were found to be sufficient for convergence of the solution for the cases examined.

After the CFD/CSD iterations are complete, acoustic computations are performed. Blade surface pressures and elastic blade motion are extracted from the CFD/CSD results by an interface code, "overflow_to_wopwop3" for use in the Ffowcs Williams-Hawkings solver, PSU-WOPWOP. PSU-WOPWOP then computes rotor impulsive / discrete frequency noise. It should be noted here that previous noise calculations of this type do not include a fuselage in the calculations. Here, because the fuselage/sting is included in the OVERFLOW2 calculations, the blade surface pressures and resultant elastic blade motions include the effect of the fuselage. However, the acoustic scattering of the fuselage is still not accounted for in this procedure. This topic is one of future study with a noise scattering method.

CFD

OVERFLOW2 [Ref. 15] is a structured grid CFD, Navier-Stokes solver capable of computing steady-state or time-accurate flowfields around multiple rigid bodies. These bodies can be either stationary, moving, or a mixture of both. It contains several solution procedure options for central difference and upwind computational schemes of various orders. There have been a number of variants and versions of the OVERFLOW2 code developed and used by a number of organizations in the last decade. To clarify and place into context the current effort, a brief history and description of some of these versions follows.

Development of the original version of OVERFLOW began at NASA Ames Research Center. Originally OVERFLOW was intended for application to flowfield calculations on the Space Shuttle [Ref. 16]. The methods used and code developments made were general enough that it rapidly found application in many areas of aerodynamics.

In the mid-1990s, researchers at NASA Ames Research Center and the U.S. Army Aeroflightdynamics Directorate (Army-AFDD) made modifications to OVERFLOW with intent to apply the new capabilities to rotorcraft problems. This modified version was became known as OVERFLOW-D [Ref. 17]. It added a number of unique features such as automatic off-body grid generation, dynamic overset grids for moving rigid bodies, scalability across multi-processors, etc. This development was parallel to, but separate from, the continued development and improvement of "standard" version of OVERFLOW maintained at NASA Langley Research Center. In the early 2000s, the standard OVERFLOW code was merged with the OVERFLOW-D code, thus creating OVERFLOW2.

Shortly after this "standard" version of OVERFLOW2 was created, researchers at Army-AFDD began adding additional rotorcraft specific capabilities to OVERFLOW2. For this paper, this Army-AFDD modified version of the code will be identified as "OVERFLOW2-ARMY" [Ref. 13, 14, 18, 19]. These modifications included a "co-processing" capability to extract grid and solution subsets during a time accurate calculation and the ability to include elastic motion of rotor blades from externally provided information. As with OVERFLOW-D, these additional capabilities were made in parallel to, but relatively separate from, the continued development of the standard version of OVERFLOW2.

In a similar but separate effort from the Army-AFDD effort, DARPA began its Helicopter Quieting Program (HQP). One of the HQP research teams began its work with OVERFLOW2-ARMY and made additional modifications. For this paper, this version of the code will be identified as the "OVERFLOW2-DARPA". These modifications included a number of new turbulence models and an additional co-processing capability to extract information on user-supplied two-dimensional surface grids (known as "Acoustic Data Surfaces" or ADS) embedded in the flowfield.

During the period of time when the OVERFLOW2-ARMY and OVERFLOW2-DARPA codes were being developed, improvements and enhancements continued to be made to the standard version of the OVERFLOW2 code. Though the OVERFLOW2-ARMY and OVERFLOW2-DARPA modifications added significant new capabilities to their respective version of OVERFLOW2, the modifications were implemented in a manner that made it difficult to update the underlying solver to maintain compatibility with the standard version of OVERFLOW2.

The present work starts with a current version of OVERFLOW2 (version 2.1s) and integrates the capabilities of (1) elastic blade motion, (2) ADS extraction, and (3) co-processing into the underlying solver. Though the capabilities were "extracted" from the OVERFLOW2-ARMY and OVERFLOW2-DARPA code versions, the insertion of these capabilities into version 2.1s required substantial modifications and updates to the methods previously implemented (programmed). For example, though the ADS extraction method was previously implemented in OVERFLOW-DARPA, differences between the underlying OVERFLOW2 solvers required a complete re-write of the actual programming. Another example is that prior versions of OVERFLOW2 on which the OVERFLOW2-ARMY and OVERFLOW2-DARPA codes were based had a "hard-coded" limit of two "fringe points" in the grid overlap regions. Recent versions of the standard OVERFLOW2 code implement the number of fringe points as a variable rather than a fixed number so that higher order methods can adjust the number of fringe points to an appropriate number. To maintain compatibility with the current solver, prior implementations had to be updated and re-coded to this new scheme.

One of the most significant changes is the implementation of all of these modifications into OVERFLOW2 version 2.1s in a manner that minimizes the number of changes required to the underlying

OVERFLOW2 solver. Minimizing the number of changes to the underlying solver in this way makes future updating of the underlying solver far simpler than before. This newly modified version of the OVERFLOW2 version 2.1s code is used for the remainder of this document and will simply be referred to as OVERFLOW2.

CFD Solution Procedure

In prior rotorcraft-related OVERFLOW2 applications [Ref. 13, 14, 17, 18, 19], the most common OVERFLOW2 solution procedure used employs a fourth-order central difference for the inviscid terms and second order central difference for all other terms (viscous terms, grid metrics, etc). Though the central difference methods produce very reasonable results, conclusions have been made and inferred [Ref. 13, 18, 19] that, for better solutions, either more grid points are needed and/or higher resolution procedures are needed. The current version of OVERFLOW2 has a number of computational schemes in addition to the central difference scheme used previously. As discussed later, both issues raised by researchers in Reference 18 are addressed here by using a dense grid and by using a higher order flow variable interpolation performed with a fifth-order WENOM [Ref. 20] is conjunction with the upwind HLLC upwind flux scheme [Ref. 20].

CSD

The Comprehensive Analytical Model of Rotorcraft Aerodynamics and Dynamics (CAMRAD-II) version 4.6 [Ref. 9] is used as the CSD analysis. This analysis models the rotor blades as a collection of finite beam segments. These segments have aerodynamic interfaces capable of incorporating aerodynamics from external sources – in this case, from OVERFLOW2. Use of CAMRAD-II in this role is discussed in detail by Potsdam, et al [Ref. 14].

Acoustic Prediction: PSU-WOPWOP

With the coupled solution converged, co-processed data extracted during the solution procedure is post-processed to obtain the blade motion and the rotor blade surface pressures. This data is further post-processed for use in the time-domain Ffowcs Williams-Hawkings (FWH) solver, PSU-WOPWOP [Ref. 20]. Previous predictions of the HART-II rotor system using similar prediction schemes used rigid blade motion and compact chordwise loading approximations in the acoustic modeling [Ref. 18]. By contrast, the current method uses blade surface pressures and elastic blade surface motions in the acoustic prediction. Time domain acoustic pressures are computed at locations of interest ("observers"). From these acoustic pressure time histories, PSU-WOPWOP computes the acoustic spectra at the observer locations. These spectra are then integrated over various frequency ranges to produce acoustic metrics, such as mid-frequency sound pressure level (SPL). These spectra will be used later in comparisons with measured data.

Wind tunnel test description

A complete description of the HART-II wind tunnel test is provided in reference 21, but a brief description is provided here for completeness. The HART-II wind tunnel test was conducted in the German- Dutch Wind Tunnel (DNW) in the fall of 2001. This comprehensive measurement effort used a 40% dynamically- and Mach-scaled model of the BO-105 hingeless rotor system with a rotor radius, R, of 2 meters. This test measured rotor vortex wake locations using 3-Component Particle Image Velocimetry (3C-PIV) and blade positions using Stereo Pattern Recognition (SPR). Balances measured gross rotor load parameters, while Kulite pressure sensors at several blade radial stations measured rotor aerodynamic loading. Only one of the radial stations (0.87R) had a chordwise distribution of pressure sensors that could be used to compute integrated sectional loading. At this section, there were 6 pressure taps distributed on the lower part of the airfoil and 11 taps on the upper surface. Integrated loading from the measured pressures was determined by van der Wall, et al [Ref. 21, 22] assuming a piecewise constant pressure distribution.

Acoustic pressure was measured using a microphone array located approximately 1.1R below the rotor hub. This array was traversed to obtain acoustic pressure measurements over the entire 1.1R plane below the rotor measurement plane. The plane spanned approximately 2R fore and aft of the rotor hub, and approximately 1.35R laterally to either side of the rotor hub. The effects on noise and vibration of Higher Harmonic Control (HHC) were studied. The HHC was implemented as particular motions of the swashplate at frequencies higher than those required for collective and cyclic pitch. The resultant blade pitch motion due to this higher harmonic swashplate motion was at a frequency equivalent to 3 cycles per rotor revolution ("3P") and a nominal 3P blade pitch amplitude of 0.8°. The phasing of this equivalent 3P HHC blade pitch was incremented in steps of 30° of one cycle for the entire cycle; therefore, 11 conditions were measured for a complete phase angle sweep of 3P HHC pitch. In this paper, a phase angle increment of 60° of one cycle is used due to computational restraints and limits.

There are three specific cases that have been studied extensively by many researchers in the last few years. These cases are (1) the baseline ("BL") case with no HHC, (2) the minimum noise ("MN") case, and (3) the minimum vibration ("MV") case. Note that the MN and MV cases are subsets of the cases examined here; however, they are specifically identified to help associate these cases with previous work by others. (It should be noted that the designations MN and MV are historical. They were coined during the HART-I effort and were identified with specific 3P phase angles of that test. These same phase angles in the HART-II effort are still identified as MN and MV cases, even though they do not produce the minimum noise and minimum vibration for the HART-II rotor [Ref. 23].)

In addition to the descent condition concentrated on during the HART-II effort, loading and acoustics were measured for different rotor angles of attack (i.e., different shaft tilt angles). To show the sensitivity of the current computations to angle of attack changes, two of these shaft tilt angles are shown - one tilt more forward than the descent case and one more aft.

Computational Grid

The full HART-II configuration (Figure 2) including rotor and wind tunnel sting support are modeled. Figure 3 shows the surface on which the computational surface grids and volume grids were developed. The HART-II rotor blade is a rectangular planform with a NACA 23012 airfoil, modified with a small rectangular tab along the trailing edge – all of which are modeled in the computations. The section of the blade inboard of the root cut-out is modeled as a section that tapers to an oval. This oval is approximately the same size as the structure that attaches the blade to the hub. Without this tapered section, strong root vortices would be artificially generated in the solution by the abrupt end of the computational grid at the root cut-out section.

On the wind tunnel sting geometry, a non-rotating cylindrical grid is used to mimic the presence of a rotor hub. There is a gap between this cylindrical hub grid and the inboard end of the blade to accommodate independent motion of each of the rotor blades. The downstream section of the sting is increased in size to approximate the increase in size of the actual sting. The actual wind tunnel sting was attached to the wind tunnel floor well downstream of the rotor; however, this attachment is not modeled in the computations. Instead, the end of the sting is capped by a hemispherical surface. This approximation is reasonable because the distances between these structures and the rotor are large; therefore, their effect should be minimal.

The "near-body" volume grids extend approximately 1 chord off of the surface grids. The background Cartesian grids in which this configuration is immersed have a uniform spacing of 0.1 chords; this grid spacing is based on findings by Lim, et al [Ref. 13, 19]. The remaining Cartesian background grids are automatically generated by OVERFLOW2 and extend approximately 25 rotor radii in all directions. These parameters result in a fairly dense grid of nearly 69 million grid points. Because these grid parameters were determined based on previous grid studies [Ref. 13, 19] and are combined with higher order methods, no additional grid refinement study has been performed.

Prediction: Loading

Baseline Case

Blade surface pressures were measured at the 0.87R radial station and are typically integrated into a blade sectional loading, conventionally presented as a normal force coefficient multiplied by the Mach number squared (C_NM^2). Figure 4 shows the measured C_NM^2 and the predicted C_NM^2 as a function of rotor azimuth (in degrees).

As noted above, the measured loading is computed by integrating the blade surface pressures assuming a piecewise constant surface pressure. The predicted loading is computed using the same method using the predicted surface pressures. However, there are far more surface pressure data points in the prediction than in the measurements due to the limited number of pressure sensors. This difference in the number of surface data points can lead to an error in the integrated loading value. The following paragraphs examine this issue for the BL case.

The line labeled "Predicted (Full)" in Figure 4 is the prediction where all points on the chord are used in the integration scheme. Note that there is an under-prediction of the mean value of C_NM^2. This under-prediction has been noted by other researchers. To date, no explanation for this difference has been conclusive. One possible explanation is a difference in integration methods mentioned above. To test this speculation, predicted surface pressure data has been extracted at the locations coincident with the blade pressure taps and has been integrated with a piecewise constant pressure assumption as was done for the measured data. The result of this is shown in Figure 4 with the line labeled "Predicted (Partial)". There is some improvement to mean value of C_NM^2 (particularly between $\psi = 0$ and 180°) when the predicted data is integrated this way and does not appear to degrade the unsteady loading features. This "partial" integration for this re-examination considered the already trimmed quantities which were determined by the coupled solution using the full integration method. It is speculated that, if the partial integration method were used for the entire iteration process, the remainder of the differences might be resolved. Alternatively, to test this speculation, all of the measured data could be re-processed by integrating the surface pressures using a higher order integration method (linear, cubic spline, etc). These are left to future research efforts.

Because (1) most cases examined to date have a similar mean offset in the measured versus predicted C_NM^2, (2) this offset does not appear to affect the unsteady pressures, and (3) the unsteady pressure (loading) affects the acoustic results the strongest, for the remainder of comparisons in this document, the predicted C_NM^2 is computed with the full chordwise pressure integration and the respective mean values for all measured and predicted C_NM^2 are removed.

The measured data and predicted results with the mean loading values removed for the BL case are shown in the right hand side of Figure 4. Both on the advancing ($0° < \psi < 180°$) and retreating ($180° < \psi < 360°$) sides of the rotor disc, the number magnitude and location of the unsteady loading (BVI) events are well matched, as is the low frequency loading. Compared to previous literature, the combination of a dense grid and higher order method appears to have improved the loading predictions for both low and mid-frequencies.

Shaft Tilt Variations

Measurements were also obtained at different shaft tilt angles, α_s, of the rotor during the HART-II effort. These non-HHC cases were examined using the BL case tunnel velocity at shaft angles, α_s, ranging from 5.4° forward to 11.4° aft. To determine the sensitivity of the current prediction method to shaft tilt, two additional shaft tilt angles are examined: one representing a shallower descent angle (α_s = 2.3°) than the BL case and one representing a steeper descent angle (α_s = 11.4°) than the BL case. Measurements and predictions are shown in Figure 5 for these two additional shaft tilts. Predictions show that, as is with the measured data, the steeper descent (α_s = 11.4°) shows multiple small unsteady events in the first rotor quadrant (0° < ψ < 90°). This is indicative of the wake approaching the rear of the rotor disc well aft of the hub. The shallower descent (α_s = 2.3°) shows fewer BVI loading events compared to the BL case; however, these BVI are more forward on the rotor disc than in the BL case. This is indicative of the wake traversing through the rotor disc earlier, and possibly quicker, than in the BL case. Encouragingly, the location, number, and magnitude of the BVI events follow the trends of the measured data.

HHC Phase Sweep

The experiment included a 3P HHC phase sweep in which the 3P HHC amplitude was held constant, but phase angle of the HHC input was varied. The following equation defines the 3P HHC pitch angle that is superimposed on the collective and cyclic pitch schedule:

$$\Theta_{3PHHC} = A\cos(3\psi + \phi)$$

Here, A is the 3P HHC amplitude with a constant value of 0.8°, ψ is the azimuth angle in degrees, and ϕ is the 3P HHC phase angle in degrees. In the experiment, the phase angle was varied from 0° to 360° in increments of 30°. For the predictions herein, a subset of the measured phases (60° increments) is examined. Figure 6 shows the measured and predicted C_NM^2 results (with the mean values removed) for 3P HHC phases of 0, 60, 120, 180, 240, and 300°. To relate these phases to previous literature, the MV case has a phase angle of 180°, whereas the MN case has a phase angle of 300°. For nearly all of these cases, the major features of the measured data are predicted. The low frequency features which are primarily due to the rotor blade HHC pitch are well tracked. In general the peak-to-peak amplitudes, number, and location of the measured and predicted BVI events on both the advancing and retreating side compare well.

Prediction: Loading Derivative

Shaft Tilt Variations

While the C_NM^2 loading computations show good agreement above, it is the time rate of change of loading that is one of the primary drivers for acoustics. Based on this, one indicator of the suitability of this prediction method for computing impulsive noise is time derivative of the loading seen in previous sections. Using the azimuth angle as the time variable, the time derivative of the measured and predicted C_NM^2 is presented. Figure 7 shows the azimuthal (time) derivative of loading for the three shaft tilt cases. It is seen that the BVI loading events on both the advancing and retreating sides are well captured in amplitude, number, and location. It is also important to note that the changes in the BVI events with respect to variations in shaft tilt are well tracked in the predictions.

HHC Phase Sweep

Similar to the previous section, Figure 8 shows the time variation of azimuthal loading derivative as a function of the HHC phase angle. In general it is seen that the BVI events are relatively well captured in amplitude, number, and azimuthal location. It is again important to note that the measured changes in the BVI events with respect to variations in HHC are tracked well by the predictions.

Though the predictions appear to track changes in conditions well, there are a few discrepancies to be noted. For example, there are BVI events in the measured data which show very sharp loading spikes. This is seen, for example, near the 70° azimuth angle in the MN case (phase = 300°) where the measured data contains a very large spike in the loading. Though the predictions match the location and number of events well, the large spike itself is under-predicted. It is speculated that, even though a dense grids and higher order methods are being used; an even denser grid and/or higher order method might be needed to better capture these rather sharp spikes in loading.

Prediction: Wake

As discussed in the introduction, past efforts to accurately predict BVI loading and noise using comprehensive analyses placed a heavy reliance on vortex wake modeling and their empirically determined vortex core sizes. Regarding CFD methods, it is often stated that they cannot maintain a vortex structure for more than a short period of time due to high dissipation. While this is true of past CFD methods which use highly dissipative schemes, recent schemes – such as the ones used in the current work – are making it possible to maintain wake structures for long periods of time. Lim, et al [Ref. 19] showed that wake geometry predicted by coupled CFD/CSD methods can do a good job of predicting wake trajectories over the rotor disc, as compared to measured PIV and flow visualization data. The current section does not provide the level of detail

presented by Reference 19, but instead intends to show qualitatively that wake information and features can retained in the simulation for a long period of time, with proper arrangement of grids. Figure 9 shows the wake structure for the BL and MN cases as iso-surfaces of the 2nd invariant of the velocity gradient tensor (*i.e.*, the "Q-criterion" [Ref. 24]).

Due to the wind tunnel sting being retained in the calculations, the "level-1" inner, dense Cartesian grid extends well downstream of the rotor system. This dense inner grid combined with the higher order and upwind methods allows the wake to be retained for a much longer distance. Flow visualization from the HART-II effort indicates that the 2nd rotor quadrant of the BL case has a single vortex emanating from the tip and that the MN case has a pair of counter rotating vortices – one at the blade tip and one inboard. Figure 9 also shows that the BL case has a single tip vortex generated at the tip, qualitatively consistent with measurements [Ref. 22]. Also the predicted MN case contains a vortex generated at the tip (labeled "A" in the figure) and one generated inboard (labeled "D" in the figure). Further investigation also reveals that these vortices are counter-rotating relative to one another's direction. Specifically, the tip vortex ("A") rotates is in a direction that indicates that the loading near the tip is negative and the inboard vortex ("D") rotates in a direction opposite to the tip vortex. These flowfield features are qualitatively consistent the experimental data. More detailed comparison of these wake features with the wake visualization and PIV from the HART-II effort (in the manner of Reference 19) is left for future research.

Prediction: Mid-Frequency Noise

Introduction

Using the predicted surface pressures and blade motion from the coupled CFD/CSD solution above, the acoustic pressure time histories are computed on a plane below the rotor; this plane corresponds to the plane mapped by the microphone array in the HART-II effort. Typical presentation consists of contour maps of un-weighted sound pressure levels (SPL) integrated over various frequency ranges. For examination of noise associated with BVI events, an SPL metric integrated from the 6th to the 40th blade passage frequency is used and is labeled "Mid-Frequency SPL". Reference 22 discusses two methods to obtain this metric from the acoustic pressure time histories: time averaged spectra and frequency averaged spectra. The latter, labeled "BVISPL-SA" in Reference 22, is used for all measured data here.

Figure 10 shows a schematic, or key, for the noise contour maps shown in Figure 11 and Figure 12. The circle in Figure 10 indicates the 2 meter rotor radius. The notional contour map is on a plane 2.215 meters under the rotor and spans 2 meters forward of the hub, 2 meters aft of the hub, and 1.35 meters laterally to either side of the hub. The tunnel velocity direction is indicated, as is the dB scale.

Shaft Tilt Variations

Figure 11 shows the un-weighted mid-frequency SPL noise metric for the three shaft tilt angles considered above. Below the rotor, the BL case shows good correlation on both the advancing and retreating sides of the plane. The noise levels are predicted well, as are the locations of the noise peaks. In prior research using solely comprehensive analyses, it has been difficult to predict the rapid decrease in noise in the forward, retreating side of the microphone plane; however, the present method appears to capture this decrease well. For the shallower descent (α_s = 2.3°), the measured shift of the noise toward the forward part of the rotor disc is matched well, though the peak level is lower than measured. For the steeper descent (α_s = 11.4°), the shift of the noise toward the advancing side aft of the rotor is captured, but there is an extraneous predicted noise region almost directly under the rotor. The cause of this particular region is unknown at this time. Though the airloads and resultant noise include the effect of the fuselage, the acoustic scattering/absorbing effects of the foam covered sting are not included as yet. This could be a contributing factor to some of these discrepancies. With the exception of this region, predicted features of the directivity pattern, including relative changes in levels, are encouraging.

HHC Phase Sweep

Figure 12 shows the mid-frequency SPL metric for the HHC phase sweep cases. Examining these cases as a whole, the general predicted trends follow the measured trends. For example, the measured noise for the 0° phase angle case has the noise concentrated under the forward part of the rotor disc, as does the predicted case. The directivity of the 60° phase angle case is not quite as well predicted as the 0° case, but the area spanned by the high noise levels is similar. Also, the measured trend of high noise region shifting laterally to the advancing side is emulated. The 180°, 240°, and 300° cases match the measured trends well.

Maximum BVI Noise Trends

The figures in the previous section allow viewing of the trends of the noise directivity with respect to changes in HHC phase angle. For a more detailed quantitative examination, the maximum mid-frequency SPL is extracted from the measured data and from the predictions and plotted in Figure 13. It is seen that there are HHC phase angles at which the maximum noise level increases and some at which it decreases. The predictions match the trends well with respect to HHC phase angles and values of maximum mid-frequency SPL. Comparing absolute value of the difference between the measured and predicted maximum mid-frequency SPL, it can be seen that largest discrepancy at any phase angle is less than 1.5 dB – most are less than 1.0 dB.

Also plotted in Figure 13 is the difference between the maximum mid-frequency SPL and that of the BL case. For the measured difference, the measured BL case is used; for

the predicted difference, the predicted BL case is used. Presenting the data this way provides an examination of differences due solely to inputs of HHC for measured and for predicted data, respectively. It is seen that the changes in the predictions with respect to HHC phase angle track very well with the trends of the measured data.

Further Applications

Considering the loading and noise predictions shown above, the current scheme is quite encouraging and shows promise as a first principles method for computing impulsive noise for rotorcraft. Using a method in which one has confidence in the noise prediction capabilities, many other applications are possible. For example, one could consider and examine the effect of, say 3P HHC, on community noise metrics to determine if the noise reduction potential is worth the investment required to implement on a flight vehicle.

To perform such an analysis, noise could be calculated on a semi-spherical surface of observers underneath the rotor for various cases. These acoustic semi-spheres could be placed in a database for use in the RNM code, discussed in the Background section above. Community noise metrics could then be computed, analyzed, and compared as needed. This effort is a task left for future research.

Conclusions

Results from recent work under the NASA SRW Project have been shown. Comments and conclusions are as follow:

- A CFD/CSD/Acoustic prediction method using recent versions of OVERFLOW2, CAMRAD-II, interface codes, and PSU-WOPWOP have been used to predict loosely coupled solutions for a series of HART-II wind tunnel cases.
- It is seen that the prediction method captures well many of the details of the C_NM^2 loading at the 0.87R spanwise blade station, as well as the time derivative of C_NM^2. Based on these loading data, the number, location, and relative strength of BVI events overall are captured well using these first principles analyses.
- Qualitative wake geometry features are captured in the current method. Specifically, in the 2nd rotor quadrant, the BL case has a single tip vortex and the MN case has two counter rotating vortices – one at the tip and one inboard.
- Using the predicted loading in the form of blade surface pressures and the elastic blade motion, impulsive noise predictions using PSU-WOPWOP show generally good agreement for mid-frequency SPL noise metrics.
- The measured trends of increasing and decreasing noise, as well as the noise directivity changes, are well reproduced for both shaft tilt variations and variations in 3P HHC inputs of the HART-II rotor.
- Changes in the maximum mid-frequency SPL values with respect to HHC phase angles are well represented. Absolute predicted maximum mid-frequency SPL values match within 1.5 dB of measured values for all HHC phase angles.

Acknowledgements

This work was performed in support of the Fundamental Aeronautics Program under the NASA Subsonic Rotary Wing (SRW) Project. Computations were performed primary on the NASA Columbia Supercomputer.

The author would like to thank Dr. Pieter Buning and Dr Joon Lim for invaluable discussions of OVERFLOW2, Dr. Berend van der Wall for discussions of HART-II data, Mr. Mark Potsdam for discussions on elastic blade modifications to OVERFLOW2, Dr. Ken Brentner and Mr. Chris Hennes for discussions related to PSU-WOPWOP.

In addition, the author would like to thank the entire HART-II test team for providing an invaluable dataset for prediction method comparisons.

References

1. Brooks, T.F., Boyd, Jr., D.D., Burley, C.L., Jolly, Jr., J.R.: "Aeroacoustic Codes for Rotor Harmonic and BVI Noise – CAMRAD.Mod1/HIRES," Journal of the American Helicopter Society, pp. 63-79, April 2000.

2. Burley, C.L., Marcolini, M.A., Brooks, T.F.: "Tiltrotor Aeroacoustic Code (TRAC) Predictions and Comparison with Measurements," Journal of the American Helicopter Society, pp. 80-90, April 2000.

3. Boyd, Jr., D.D., Burley, C.L., Conner, D.A.: "Acoustic Predictions of Manned and Unmanned Rotorcraft Using the Comprehensive Analytical Rotorcraft Model for Acoustics (CARMA) Code System", American Helicopter Society International Specialists' Meeting on Unmanned Rotorcraft, Phoenix, AZ, January 18-20, 2005.

4. Johnson, W.: "A Comprehensive Analytical Model of Rotorcraft Aerodynamics and Dynamics, Part I: Analysis Development", NASA TM 81182, June 1980.

5. Johnson, W.: "A Comprehensive Analytical Model of Rotorcraft Aerodynamics and Dynamics, Part II: User's Manual", NASA TM 81183, June 1980.

6. Brentner, K.S.: "Prediction of Helicopter Discrete Frequency Noise – A Computer Program Incorporating Realistic Blade Motions and Advanced Acoustic Formulation", NASA TM 87721, October 1986.

7. Bridgeman, J.O., Prichard, D., Caradonna, F.X.: "The Development of a CFD Potential Method for the Analysis of Tilt-Rotors", American Helicopter Society Technical Specialists' Meeting on Rotorcraft Acoustics and Fluid Dynamics, Philadelphia, PA, October 1991.

8. Conner, D.A., Page, J.A.: "A Tool for Low Noise Procedures Design and Community Noise Impact Assessment: The Rotorcraft Noise Model (RNM)", Heli Japan 2002, Tochigi, Japan, November 11-13, 2002.

9. Johnson, W.J.: "CAMRAD-II: Comprehensive Analytical Model for Rotorcraft Aerodynamics and Dynamics", Volumes 1-9, Johnson Aeronautics, Palo Alto, CA, 2007.

10. Brentner, K.S., Perez, G., Brès, G.A., Jones, H.E.: "Toward a Better Understanding of Maneuvering Rotorcraft Noise," American Helicopter Society 58th Annual Forum, Montréal, Canada, June 11-13, 2002.

11. Hennes, C., Lopes, L., Shirey, J., Erwin, J.: "PSU-WOPWOP 3.3 User's Guide", The Pennsylvania State University, June 28, 2007.

12. Datta, A., Nixon, M., Chopra, I.: "Review of Rotor Loads Prediction with the Emergence of Rotorcraft CFD", Journal of the American Helicopter Society, Volume 52, Number 4, October 2007.

13. Lim, J.W., Nygaard, T.A., Strawn, R., Potsdam, M.: "Blade-Vortex Interaction Airloads Prediction Using Coupled Computational Fluid Structural Dynamics", Journal of the American Helicopter Society, Volume 52, Number 4, October 2007.

14. Potsdam, M., Yeo, H., Johnson, W.R.: "Rotor Airloads Prediction Using Loose Aerodynamic/Structural Coupling", Journal of Aircraft, Vol 43 (3), May-June 2006, pp. 732-742.

15. Nichols, R.H., Tramel, R.W., Buning, P.G.: "Solver and Turbulence Model Upgrades to OVERFLOW2 for Unsteady and High-Speed Applications", AIAA Paper 2006-2824, June 2006.

16. Buning, P.G.: Private communications with the author.

17. Meakin, R.L., Wissink, A.M.: Unsteady Aerodynamic Simulation of Static and Moving Bodies Using Scalable Computers", AIAA Paper 1999-3302, 14th Computational Fluid Dynamics Conference, Norfolk, Virginia, June 28 – July 1, 1999.

18. Sim, B., Lim, J.W.: "Blade-Vortex Interaction (BVI) Noise and Airloads Prediction Using Loose Aerodynamic/Structural Coupling", American Helicopter Society 62nd Forum Proceedings, May 2007, Phoenix, AZ.

19. Lim, J.W., Strawn, R.C.: "Computational Modeling of HART II Blade-Vortex Interaction Loading and Wake System", Journal of Aircraft, Vol 45, No. 3, May-June 2008.

20. Nichols, R.H., Tramel, R.W., Buning, P.G.: "Evaluation of Two High-Order Weighted Essentially Nonoscillatory Schemes", AIAA Journal, Vol. 46, No. 12, December 2008.

21. van der Wall, B.G.: "2nd HHC Aeroacoustic Rotor Test (HART-II) – Part 1: Test Documentation", German Aerospace Center Institute Report IB 111-2003/31, November 3, 2003.

22. van der Wall, B.G., Burley, C.L.: "2nd HHC Aeroacoustic Rotor Test (HART-II) – Part II: Representative Results", German Aerospace Center Institute Report IB 111-2005/03, February 5, 2005.

23. Brooks, T.F.: Private communication with the author, February 23, 2009.

24. Chaderjian, N.: Private communication with the author, September 19, 2007.

Figures

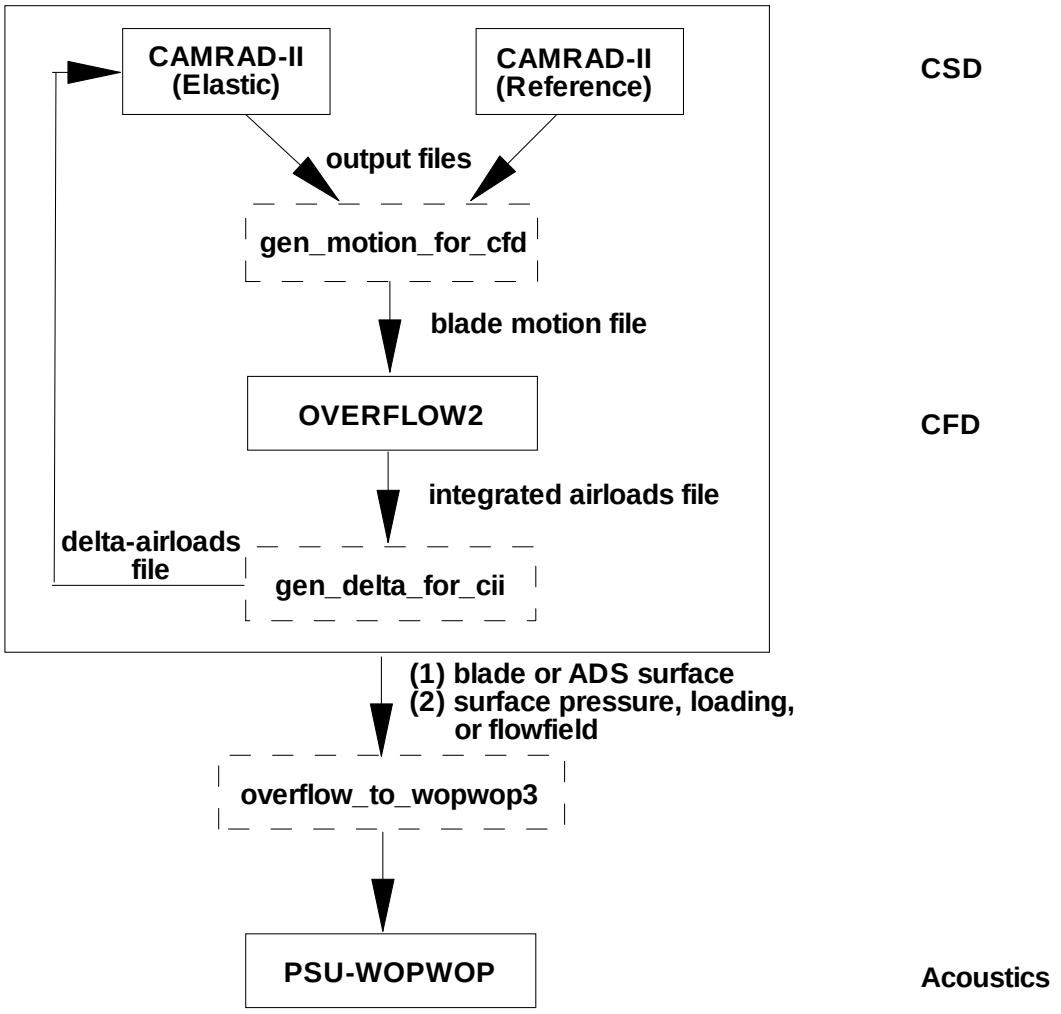

Figure 1: Schematic of present CFD/CSD/Acoustic method. Boxes with dashed lines signify interface codes. Boxes with solid lines signify codes.

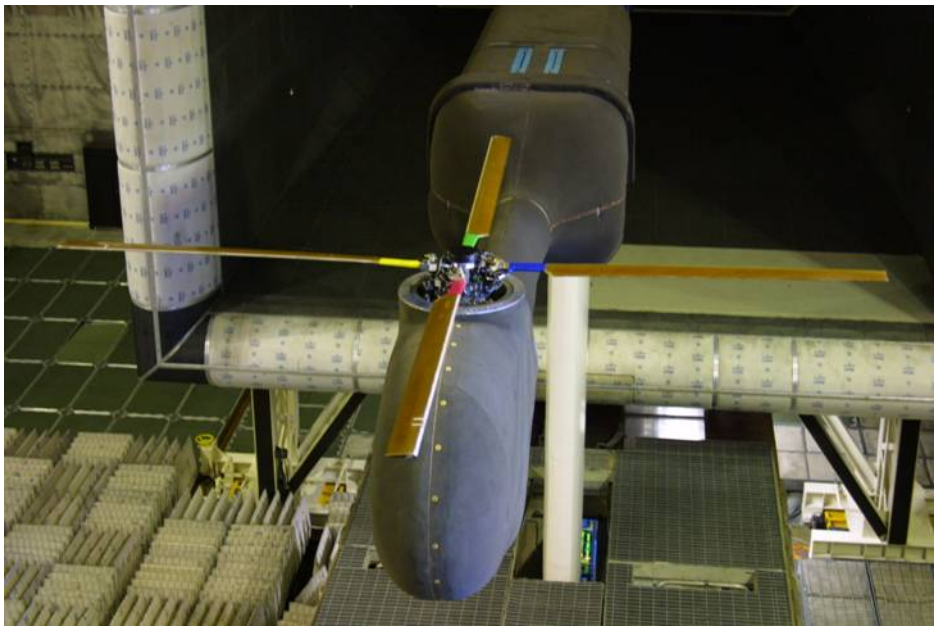

Figure 2: HART-II wind tunnel configuration.

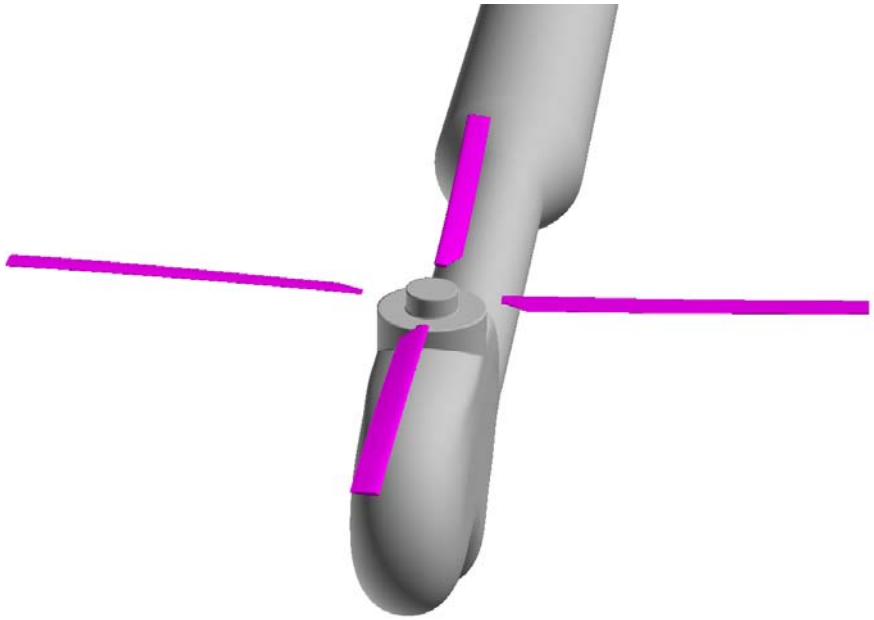

Figure 3: HART-II surface configuration for computations.

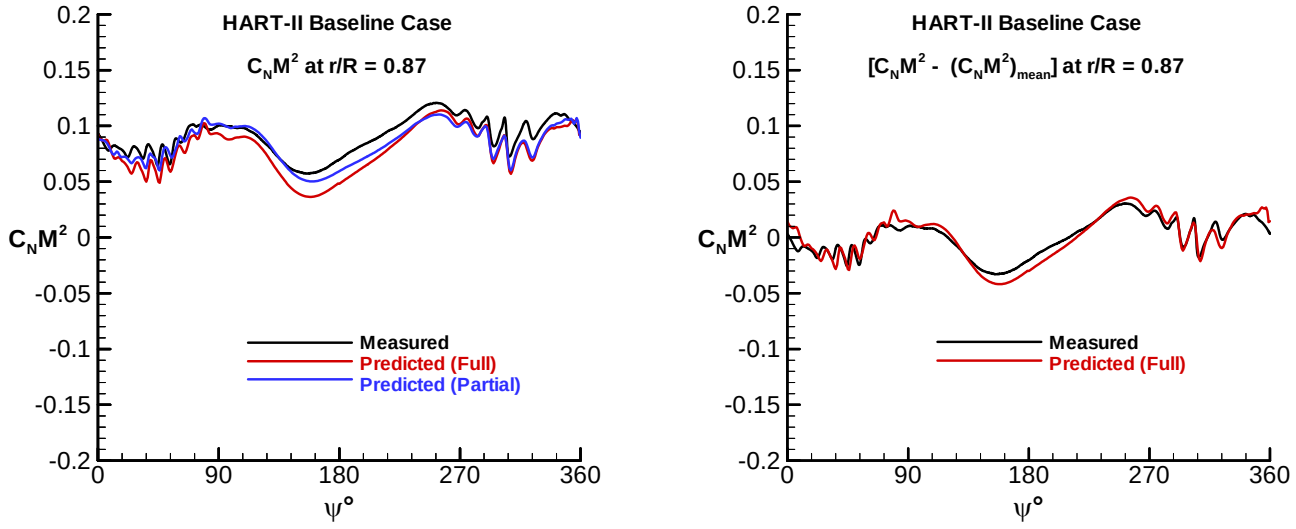

Figure 4: Measured and predicted C_NM^2. "Prediction (Full)" is the predicted integrated loading using the full chordwise pressure distribution. "Predicted (Partial)" shows the integrated loading using predicted data only at the measured pressure tap locations. Results are also shown with mean C_NM^2 removed.

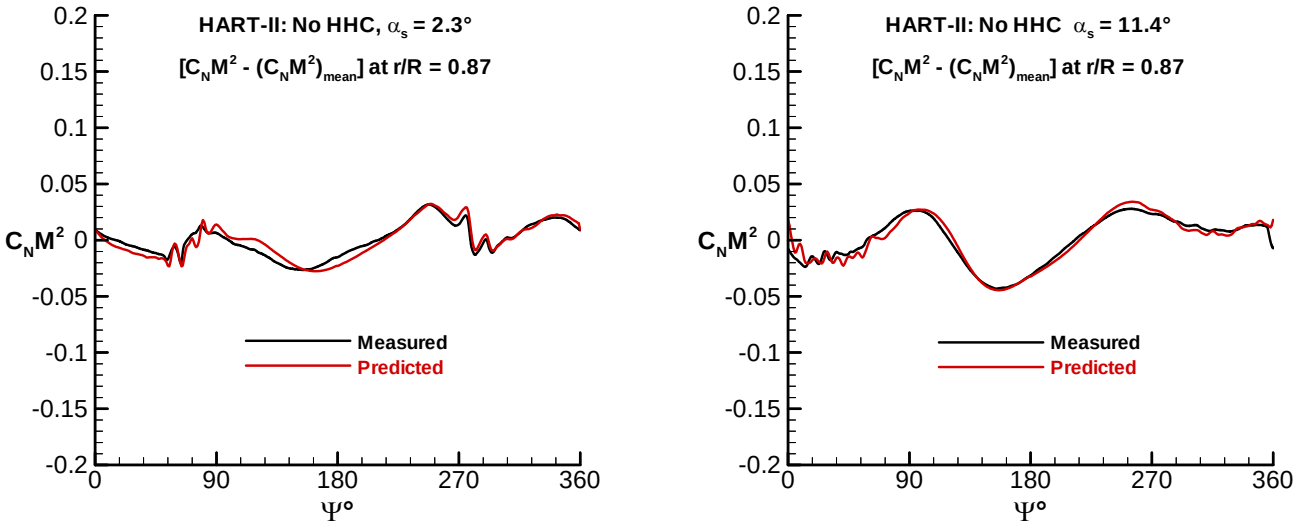

Figure 5: Measured and predicted C_NM^2 (mean values removed) for 2.3° and 11.4° aft shaft tilts.

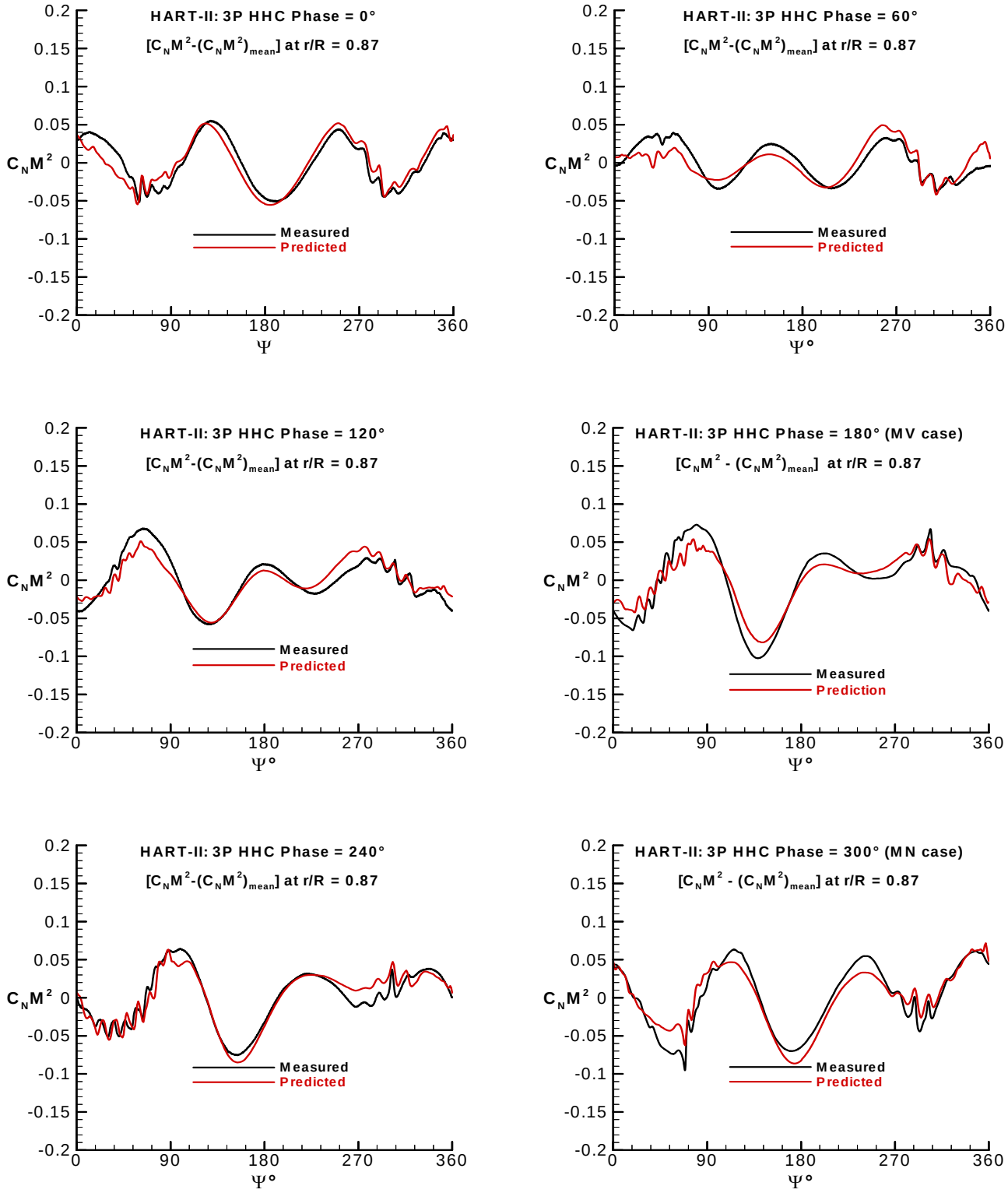

Figure 6: Measured and predicted C_NM^2 for 3P HHC phase sweep cases.

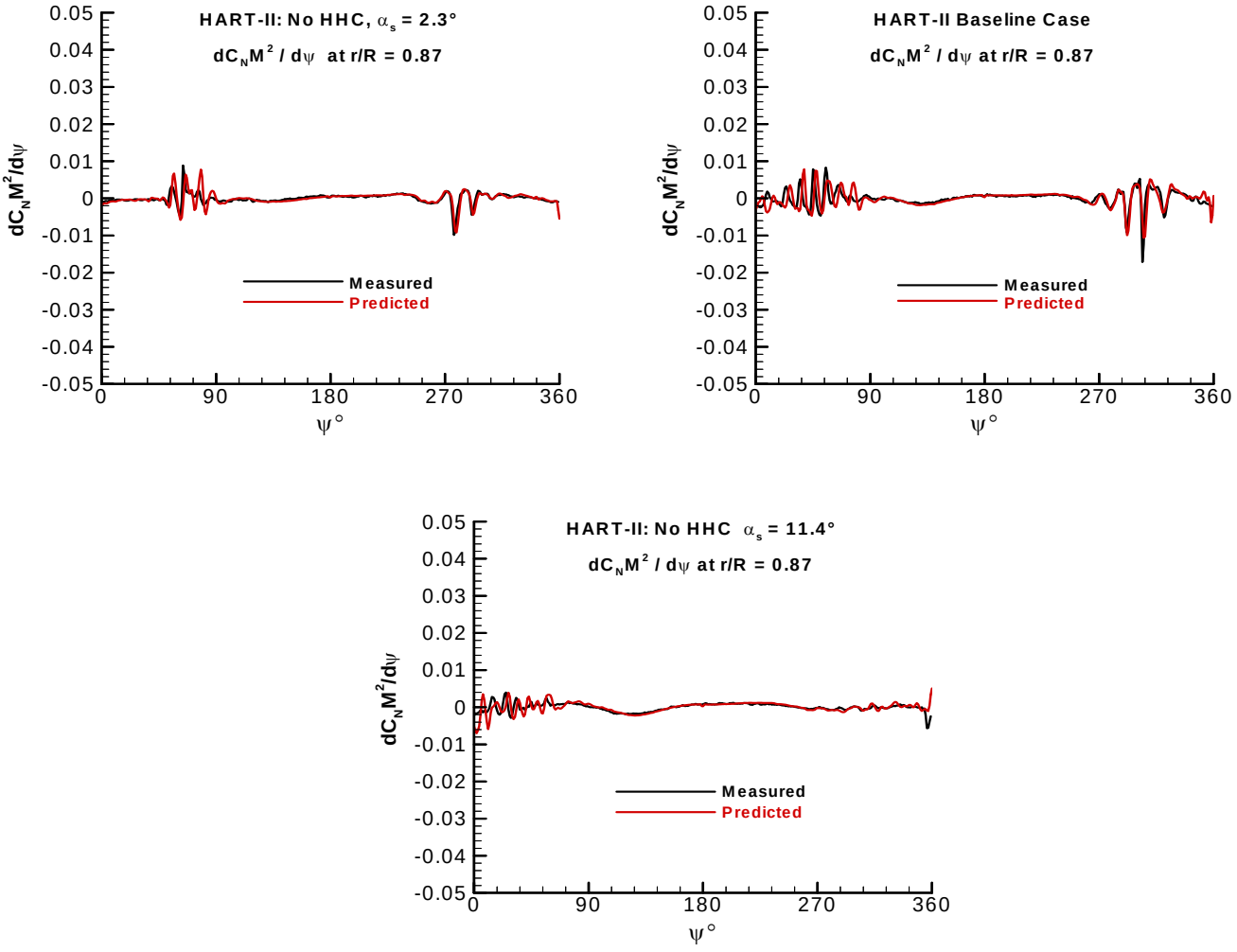

Figure 7: dC_NM^2 / dψ for shaft tilt range.

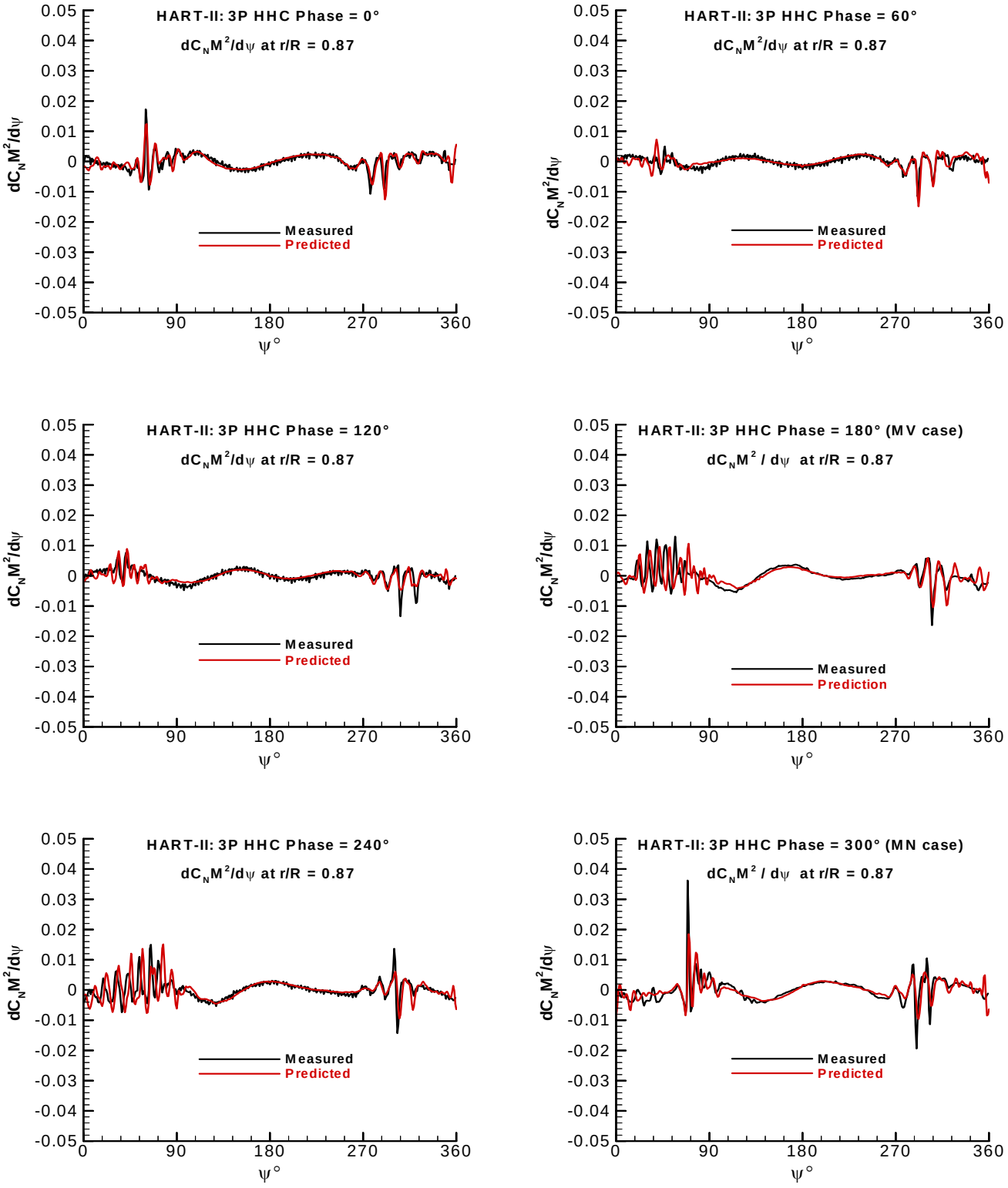

Figure 8: $dC_N M^2 / d\psi$ for 3P HHC phase sweep.

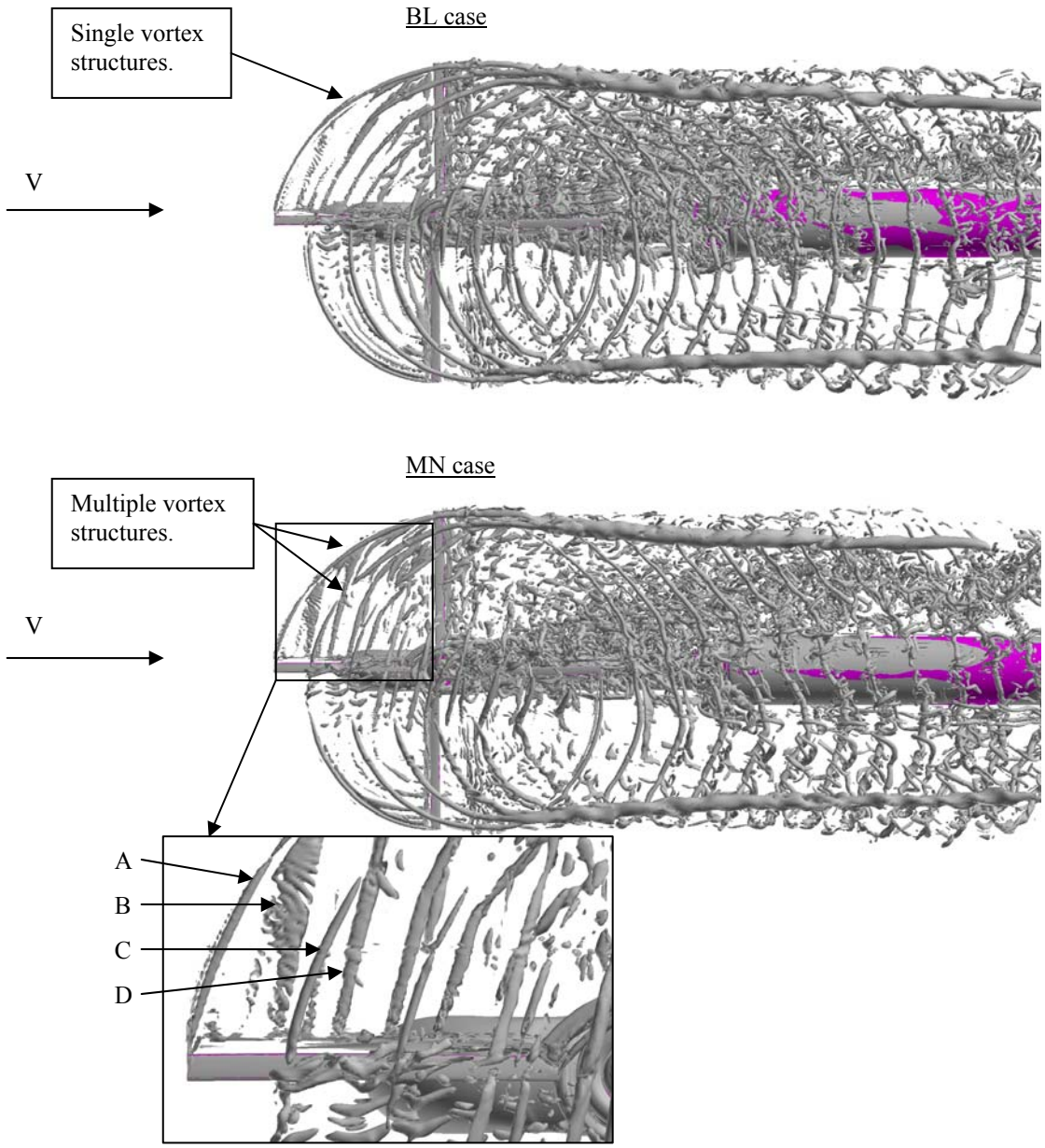

Figure 9: Iso-surface of 2nd invariant of the velocity gradient tensor (the "Q-criterion"). Feature in close up: (A) tip vortex from blade at azimuth of 90° - vorticity indicates negative loading, (B) vortex sheet from blade at azimuth of 90°, (C) tip vortex from blade at azimuth of 270°, (D) inboard vortex from blade at azimuth of 90° -- counter rotating vortex relative to vortex (A).

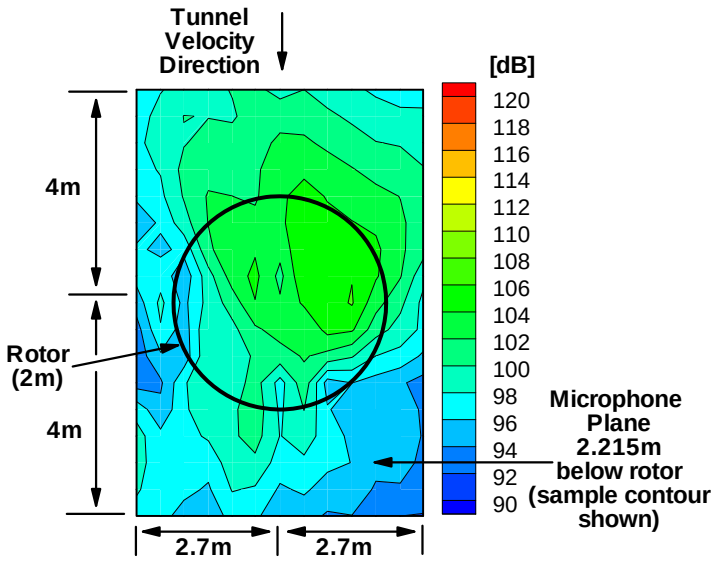

Figure 10: Schematic describing all noise contour maps in the following two figures.

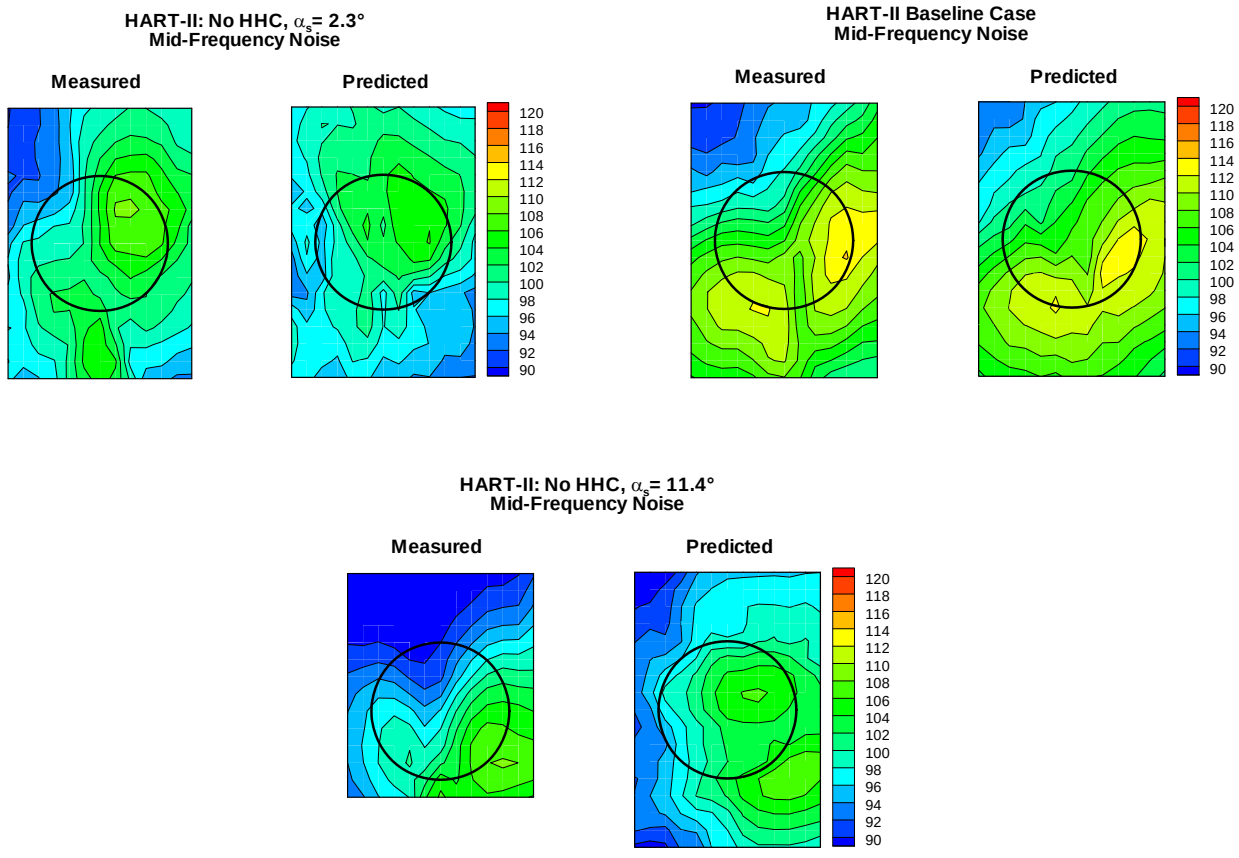

Figure 11: Measured and Predicted Mid-Frequency Noise for a range of shaft tilt angles.

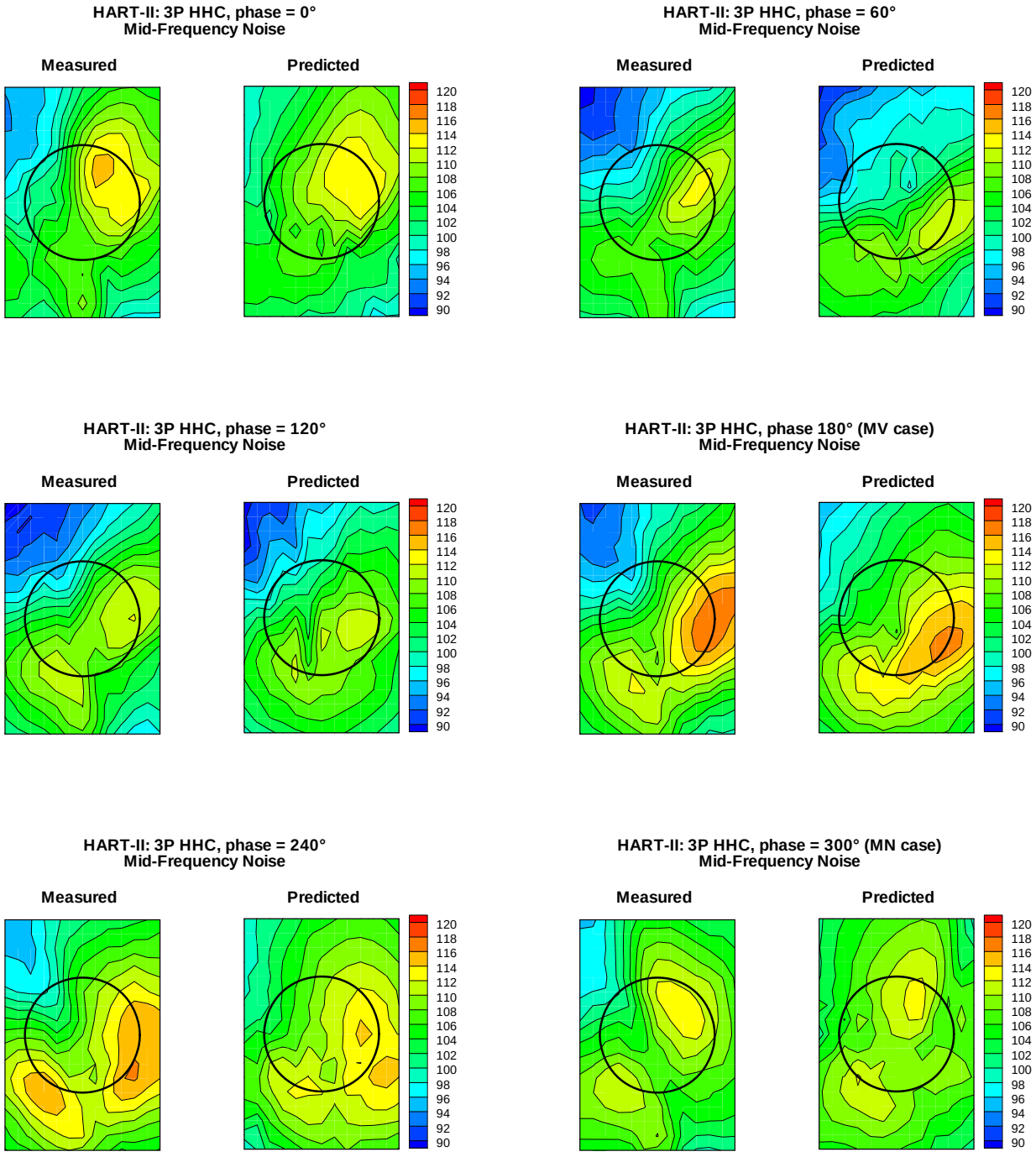

Figure 12: Measured and Predicted Mid-Frequency Noise for 3: HHC phase sweep.

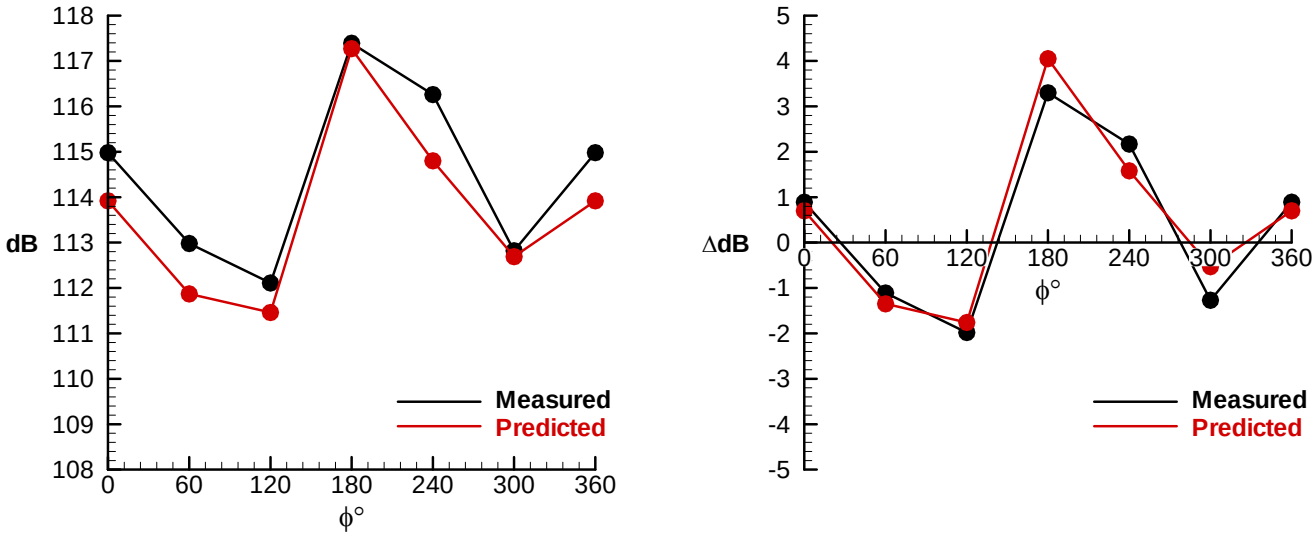

Figure 13: Maximum values of mid-frequency noise [dB] as a function of HHC phase angle. Change in the maximum values of mid-frequency noise [ΔdB] as a function of HHC phase angle (relative to the BL case).